Spaceborne High Precision Sea Surface Salinity Remote Sensing by Interferometric Radiometry

Yinan Li, Congcong Wang ⓘ, Hailiang Lu ⓘ, Guangnan Song, Xiaojiao Yang, Pengfei Li, Rongchuan Lv, Hao Li, and Wenxin Chen

Abstract—The global sea surface salinity (SSS) can be accomplished by means of the L-band microwave radiometers from space, such as European Space Agency's SMOS (soil moisture and ocean salinity) and NASA's Aquarius/SAC-D. However, the microwave imaging radiometer using aperture synthesis in SMOS mission suffers from various errors and unexpected in-orbit phenomena, which degrade SSS accuracy. To further improve SSS accuracy, a full polarization aperture synthesis microwave radiometer (FPASMR) has been proposed for China's next-generation Haiyang satellite program with two important improvements, which is composed by an L- and X-band aperture synthesis radiometer (ASR) with two dimensions. One important improvement is that the sea surface roughness and sea surface temperature are simultaneously measured by the full polarization X-band ASR, and another important improvement is that the microwave-optical receiving technology and in-orbit thermal control subsystem are employed to improve the stability of the FPASMR for reducing visibility phase errors. The system of the FPASMR is introduced in terms of L-band subsystem, X-band subsystem, and the calibration subsystem. The main specifications of the FPASMR are analyzed in terms of field of view, angular resolution, and radiometric sensitivity. In addition, the FPASMR calibration is also introduced. The FPASMR demonstrator has also been developed and a series of experiments is performed to assess the performance of the FPASMR demonstrator and the improvements in the FPASMR.

Index Terms—Demonstrator, high stability, L\X-band, microwave optical, sea surface salinity (SSS).

I. INTRODUCTION

SEA surface salinity (SSS) is an important parameter in the oceanography and climatology, which is a key indicator of the underlying processes that link the ocean circulation and hydrologic cycle [1]. The global SSS can be accomplished by means of the L-band microwave radiometers from space, such as European Space Agency's SMOS (soil moisture and ocean salinity) [2] and NASA's Aquarius/SAC-D [3]. The microwave imaging radiometer using aperture synthesis (MIRAS) is the single payload of the SMOS mission [2]. Aquarius/SAC-D [3] is a combination of active/passive L-band microwave instruments developed by the USA (NASA) and Argentina (CONAE). Up to now, the SMOS and Aquarius satellite missions have demonstrated the capability of L-band radiometry for monitoring SSS from space [4]. The scientific objective of SMOS mission is to provide global SSS maps with an accuracy of 0.1 psu at a spatial resolution of 100 (200) km every 30 (10) days in open ocean [5]. The scientific objective of Aquarius/SAC-D is to provide global maps with an accuracy of 0.2 psu at a spatial resolution of 150 km every 30 days in the open ocean [3]. At present, SMOS and Aquarius have achieved their scientific objectives in the open ocean [6].

However, MIRAS in SMOS mission suffers from various errors and unexpected in-orbit phenomena, which cause negative effects on the SMOS brightness temperature (TB) maps and degrade the accuracy of the retrieved SSS from TB maps [7], [8]. One main error source in the retrieved SSS comes from the uncertainty on ocean surface emissivity related to the surface waves and foams [9], [10]. In SMOS or Aquarius, the auxiliary wind speeds have been considered to mitigate the wind effect on the retrieved SSS accuracy, which comes from the European Centre for Medium-Range Weather Forecasts (and the special sensor microwave imager/sounder. However, two sources of the auxiliary wind speeds have a limitation on L-band TB products in the spatio-temporal domains for SMOS and/or Aquarius [9]. Meanwhile, the visibilities in SMOS suffer from short-terms phase errors, which is due to the phase of the distributed local oscillators (LO) in SMOS is sensitive to the physical temperature variations [8].

To further improve SSS accuracy, a full polarization aperture synthesis microwave radiometer (FPASMR) has been proposed by the China Academy of Space Technology (Xi'an) for China's next-generation Haiyang (HY) satellite program [11]. FPASMR is composed by an L- and X-band aperture synthesis radiometers (ASRs) with two-dimensions (2-D). Two important improvements are considered in FPASMR to improve SSS retrieved accuracy. One aspect it that the sea surface roughness (SSR) and sea surface temperature (SST) are simultaneously measured by the full polarization X-band ASR. Another aspect is that the microwave-optical receivers and the in-orbit thermal control subsystem are employed in FPASMR to improve the stability of the instruments and reduce the visibility phase errors [8].

The rest of this article is organized as follows. The improvements in FPASMR are introduced in Section II. The system

The authors are with the China Academy of Space Technology, Xi'an 710100, China (e-mail: liyinan_cast@126.com; sunseacc@163.com; hust_lhl@163.com; songguangnan328@126.com; xiaoqiao_0709@126.com; 811061709@qq.com; roselinda_lrc@163.com; cast504_lihao@163.com; chenwx801@sohu.com).

description is present in Section III. Validation, results and discussion are performed in Section IV. Finally, the conclusion is drawn in Section V.

II. IMPROVEMENTS IN FPASMR

A. Improvement in SSR and SST Errors

On a global scale, the uncertainty in the surface brightness TB translates into an SSS uncertainty roughly as 1:2 ratio [12], [13]. In order to observe the phenomena relevant to large-scale and climatic studies, such as halosteric adjustment of heat storage from sea level, North Atlantic thermohaline circulation, and surface freshwater flux balance, an obtainable accuracy of 0.1∼0.4 psu is required over 100∼300 km in 10∼30 days [13]. It means, that the requirement of radiometric accuracy is about 0.05 K∼0.2 K [12], [13], which poses an extremely challenging task to the microwave radiometers from space.

For the microwave radiometers from space, the major error sources in the SSS retrieval algorithm come from the uncertainty on SSR and SST, and so on [12].

As one of the major error sources in SMOS or Aquarius [14], the SSS retrieval error refers to the ocean surface emission variations due to SSR. SSR is mainly caused by sea surface winds, which could result in large gravity waves, small capillary waves, and, at higher wind speeds, foam coverage of the ocean surface [15]. Accordingly, an accurate knowledge of the sea surface wind speed is necessary. Numerical simulations are performed to assess the impacts of the wind speed errors and SST errors on the SSS retrieval errors, respectively. As shown in Fig. 1, the SSS retrieval errors due to the wind speed errors (top) and the SST errors (bottom) are given with various wind speeds and various SST, respectively. It can be seen that SSS retrieval error increases as the wind speed error increases at a fixed wind speed. When the requirement of the SSS retrieval error is lower than 1 psu for single measurement, the wind speed error must be reduced to 1 m/s at least.

As another major source in SMOS or Aquarius [14], SST measurement error about 0.5 K can translate into 0.08 psu SSS retrieval error (single). Fortunately, the sea surface wind speeds and SST can be simultaneously estimated by the full polarization X-band radiometers. For the global SSS, the L-band ASR is a good candidate from space. Thus, a 2-D full-polarization L-band ASR is proposed with a 2-D full-polarization X-band ASR for the global SSS with high precision. The X-band ASR aims to simultaneously estimate SSR and SST for the L-band ASR to improve SSS retrieved accuracy.

B. Improvement in Stability of ASRs

For an L-band ASR from space, it is very difficult to achieve SSS retrieved accuracy of 0.1 psu with single snapshot. However, the accuracy of microwave measurement TB can be improved by averaging multiple snapshots due to a pixel remaining in the field of view (FOV) of an L-band ASR from space for a long time, such as in SMOS. As a result, the averaged multiple snapshots can further improve the SSS retrieved accuracy. However, there are three error and/or noise sources in the TB measurements
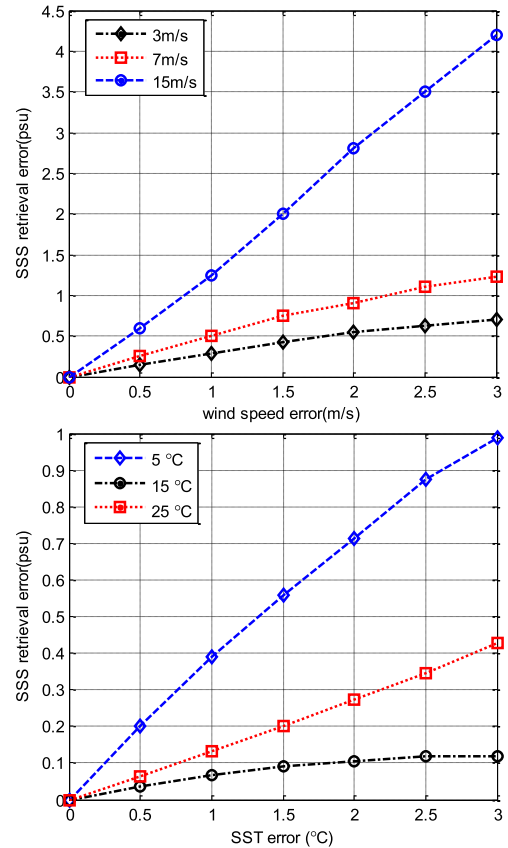

Fig. 1. SSS retrieval error due to the wind speed error with various wind speeds (top) and the SST error with various SST (bottom).

to degrade the SSS retrieved accuracy. One error source is the system sensitivity, which follows Gaussian distribution and can be reduced by averaging [14]. Another error source is calibration accuracy, which has a dependence on the absolute calibration method. The third error source is the system stability, which mainly depends on the gain drift of the receivers and/or the environment temperature variations [14]. However, the third error source cannot be reduced by averaging. Therefore, the ASRs must be exhibit a high stability during the short-term periods that a pixel remaining in FOV of an L-band ASR from space. In addition, the ASRs are also expected to exhibit a high stability during a long-term period, as long as possible [8]. As a result, the stability of the ASRs is an important factor to reduce the noises in the TB measurements to further improve SSS retrieved accuracy. As mentioned in [14], the stability requirement of the L-band radiometer from space is 0.15 K for 0.1 psu SSS monthly accuracy requirement.

In SMOS, because of the large aperture antenna size, antennas and receivers are distributed into different antenna arms. As a result, the thermal environment of the SMOS in orbit is different in each antenna arm to reduce the stability of the receiver and cause the gain and offset drifts of receivers [16]. In addition, since the distributed LO structure is employed in MIRAS, the LO temperature variations produce phase errors in the visibilities, which degrade the TB measurement accuracy and further reduce the SSS retrieved accuracy [8].
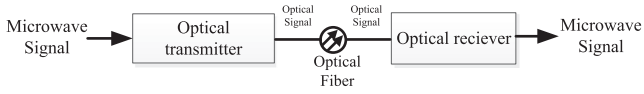
Fig. 2. Block diagram of the microwave-optical receiver.

To improve the stability of the ASRs and reduce the phase errors in the visibilities caused by LO temperature variations, the microwave-optical receiving technology is employed. In the microwave-optical receiving technology, the LO signals can be modulated to optical signals and be pasted to the optical receivers in each arm by optical fibers. Then, the optical signals can be modulated to the microwave signals by the optical signals, as shown in Fig. 2. Since the optical fibers are in sensitive to the physical temperatures, the stability of the ASRs can be improved and the phase errors in the visibilities caused by LO temperature variations can be reduced by the microwave-optical technology. As a result, the SSS retrieved accuracy can be improved.

As aforementioned, the SSS retrieved accuracy can be improved by averaging multiple snapshots, because SSS is a slowly variation parameter in the spatio-temporal domains. However, the stability of the ASRs in the microwave radiometers has an important impact on the SSS retrieved accuracy [16] and depends on the operational temperature and/or the environment temperature. To reduce the thermal temperature variations, the in-orbit thermal control subsystem is also designed in the microwave radiometers from space to maintain a constant operational temperature for each receiver, as possible.

In addition, the temperature compensation method is considered to periodically compensate the gain and offset variations of the receivers over temperature for further improving the SSS retrieved accuracy. On ground, the gain and offset are characterized over temperature, and the gain and offset sensitivity coefficients over physical temperature are accurately estimated [17], [18]. The sensitivity coefficients are also in-orbit updated in the long calibration operations [17], [18].

The gain (G) and offset (O) of each receiver at a given working temperature T in flight can be estimated by

$$G(T) = G(T_0) + S_G(T - T_0) \tag{1}$$

$$O(T) = O(T_0) + S_O(T - T_0) \tag{2}$$

in which $G(T_0)$ and $T_R(T_0)$ are the receiver gain and offset at the physical temperature T_O during calibration on ground, and S_G and S_O are the sensitivity coefficients of the receiver gain and offset over the physical temperature, respectively.

III. SYSTEM DESCRIPTION

This section is devoted to the system of the FPASMR, in which system structure, main specifications and calibration are introduced.

A. System Structure

FPASMR is constituted by an L-band ASR and an X-band ASR with full polarization measurement. As shown in Fig. 3, the model of FPASMR is given. Both L- and X-band ASR employ a "Y-shaped" array with 23 antennas per arm plus one in the
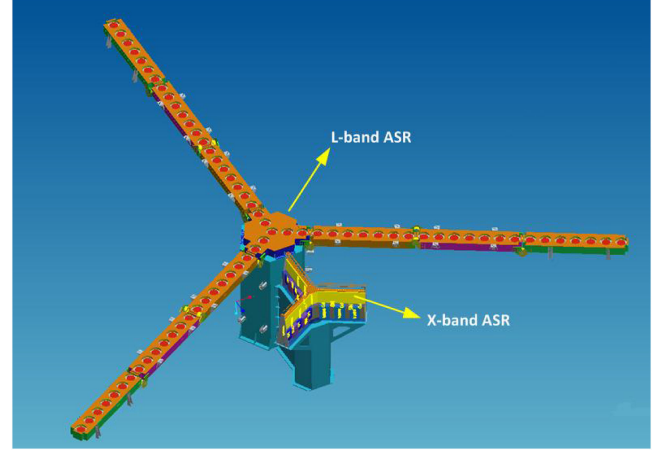

Fig. 3. Concept of FPASMR. FPASMR consists of an L-band Y-shaped ASR and an X-band Y-shaped ASR.

TABLE I
SPECIFICATION OF FPASMRs

Parameter	FPASMR	
	L-band	X-band
Center frequency	1.415 GHz	10.7 GHz
Bandwidth	20 MHz	100 Mhz
Minimum spacing	0.82	0.82
Integration time	1s	1s
resolution@655 km	20~65 km	20~65 km
Fov@655 km	≥ 800km	≥ 800km
Tilt angle	30°	30°
Snap-shot sensitivity	2.5~3.5K	1.4~2.2K
Topology of the LO	Single LO	Centralized reference clock and internal LO in each receiver
Antenna array	"Y" shaped	
Antenna numbers	70	
Polarization	V\H\3\4	
Quantization	10-bits for power measurement 1-bit for correlation	
IQ	Digital IQ	
Power measurement	Digital power measurement	
Frequency response	Digital filter	

center (total 70 antennas). Due to the large diameter of the L-band array (>8 m), it is necessary to fold the antenna arms to satisfy the available launcher volume. However, there is no consideration to fold the antenna arms of the X-band ASR due to the diameter of the X-band array antenna is about 1 m. The FPASMR system contains three main subsystems: L-band ASR subsystem, X-band ASR subsystem, and calibration subsystem. The main specification of FPASMR is shown in Table I.

1) L-Band Subsystem: The L-band subsystem employs three deployable antenna arms. Each arm is ∼4 m and divided into three segments. There are 23 antenna elements per each arm plus one in the hub. To satisfy the requirement of SSS accuracy, the stability of each receiver must be better than 0.12 K [3]. One consideration is that the thermal control subsystem is designed in each arm of the L-band ASR to maintain a constant operational temperature for each receiver, further to improve the stability of each receiver. Another consideration is that the microwave-optical technology is employed to greatly reduce the phase errors in the visibilities caused by the LO, which are seriously affected
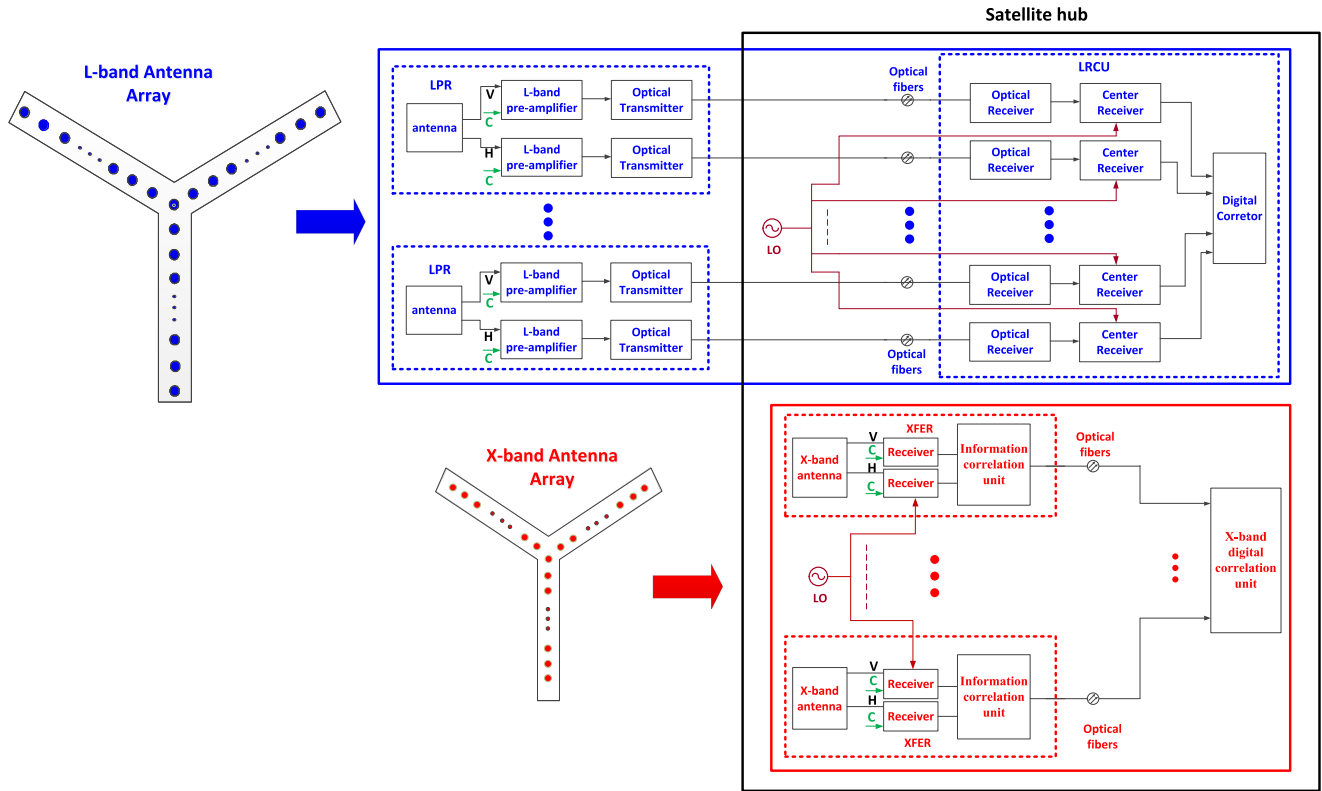
Fig. 4. Block diagram of FPASMR.

by the environment temperature variations, such as in SMOS [19].

As shown in Fig. 4, the block diagram of L-band subsystem is given. The L-band subsystem comprises 70 L-band prereceivers (LPR), an integrated L-band central receiver and digital correlation unit (LRCU). Each LPR consists of an L-band microstrip antenna with dual polarization (V and H), two L-band low noise amplifiers and two optical transmitters. Due to the attenuation of the optical transmitters about 20 dB, the gain of the preamplifiers must exceed 45 dB to ensure that there is no deterioration in the noise figure of receiver (~0.1 dB deterioration). The RF signal is modulated to optical signal by the optical transmitter (see Fig. 4) and transmitted to LRCU by optical fibers. The LRCU consists of 140 optical receivers, 140 center receivers, a centralized LO and the digital correlator (see Fig. 4).

The optical signal is received and transmitted to RF signal by the optical receivers (see Fig. 5), which consists of high speed photodetectors and broadband amplifiers. Then, after passing through the band-pass filters, mixers, low pass filters and IF amplifiers in the center receivers, the RF signals are demodulated to the IF analog signals (75 MHz), which will be digitalized by the analog-to-digital converters (ADCs) with 100 MHz in the digital correlator units. Meanwhile, the digital correlator units comprise digital power measurement systems, digital filters, and digital correlators. The IF analog signals coming from the antennas are measured by a 10-b digital power measurement system, and all the visibilities are obtained by the 1-b digital correlator.

2) X-Band Subsystem: Due to the small volume of X-band subsystem (~1 m aperture), the environment temperature
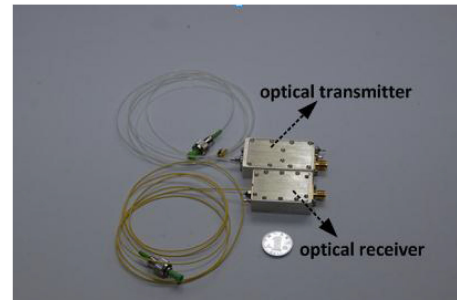

Fig. 5. Optical transmitter (upper) and optical receiver (lower).

variations are well-controlled and the phase consistency/stability of the receivers can be well-satisfied in the distributed LO topology. Thus, a centralized reference clock and an internal LO in each receiver are employed in the X-band subsystem. As shown in Fig. 4, the block diagram of X-band subsystem is also given. The X-band subsystem comprises 70 X-band front-end receivers (XFER) and an X-band digital correlation unit (XDCU).

In the X-band subsystem, each XFER employs a similar receiver topology as PAU-SA [19], [20], and each XFER comprises an X-band dual polarization horn antenna, two front-end single-band receivers and an X-band information correlation unit. The output signals of the front-end single-band receivers in each XFER are digitalized by the information correlation unit. The information correlation unit also comprises digital power measurement systems, digital filters and 1-b ADCs. Digitalizing the analog signals with 1-b can greatly reduce the systematic complexity. Then, the 1-b digital signals of XFER are
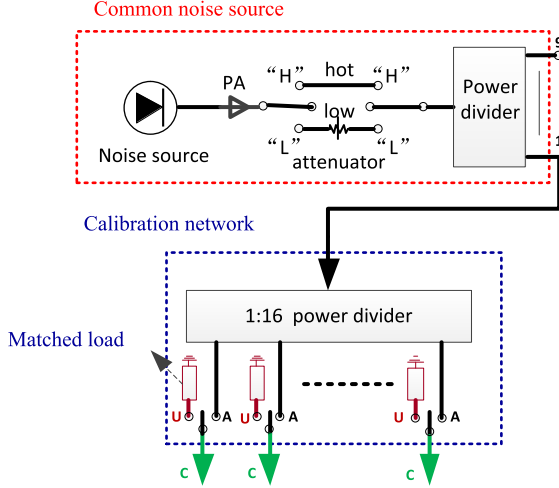
Fig. 6. Calibration subsystem in FPASMR.

TABLE II
RADIOMETRIC SENSITIVITY PARAMETERS

Subsystem	L-band	X-band
T_A	200 K	200 K
T_R	120 K	170 K
B	20 MHz	100 MHz
d	0.82	0.82
Ω_a	1.7	1.7
α_w	0.45	0.45
N_{el}	23	23
τ_{eff}	2 s/2.46	2 s/2.46

transmitted to XDCU by microwave-optical technology, and all the visibilities are obtained by the XDCU for the X-band subsystem.

3) Calibration Subsystem: The calibration subsystem in the FPASMR is similar as the calibration subsystem in SMOS, and it comprises a common noise source and a calibration network, as shown in Fig. 6. In the calibration subsystem, two levels of correlated noises (called "hot" source about 1100 K and "low" source about 320 K) generated by the common noise source are driving into the prereceivers of L-band subsystem and the receivers of X-band subsystem by the calibration network to calibrate the gain and phase of the receivers (see Fig. 4). The common noise source is constituted by a noise source, a power amplifier (PA), two switches, an attenuator, and a 1–9 power divider. The "hot" source and "low" source are provided, when the switches are connected to the "H" ports and "L" ports in sequence. The calibration network comprises a 1–16 power divider, 16 calibration switches and matched loads. The un-correlated noises are provided by the matched loads in the calibration network when the switches are connected to the "U" ports, as shown in Fig. 6.

B. Main Specifications of FPASMR

This section is devoted to the main specifications of FPASMR, which include FOV, angular resolution, and radiometric sensitivity.

1) Field of View: For an ASR, the measured visibilities are samples of the TB maps of the scene in the spatial frequency. For FPASMR, due to the Y-shaped array [see Fig. 7 (left)] employed in the L- and X-band ASR, the visibilities are sampled as follows:

$$u = \frac{\sqrt{3}}{2} \cdot d \cdot k_1 \qquad (3)$$

$$v = \frac{d}{2}(-k_1 + 2k_2) \quad k_1, k_2 \in (0 \cdots N_T) \qquad (4)$$

in which $N_T = 3N_{el} + 1$ is the total number of antennas, N_{el} is the number of each antenna arm of the Y-shaped array, and d

is the adjacent antenna spacing normalized to the wavelength. The U-V coverage is shown in Fig. 7 (middle).

For the ASR with "Y-shaped" array, the hexagonal fast Fourier transform is usually performed to retrieve the TB maps. The whole space maps into the unit circle so the TB map is a function bounded by this region. In addition, since the adjacent antenna spacing is larger than the Nyquist sampling spacing, there is some amount of aliasing [24]. As shown in Fig. 7 (right), the on-ground alias-free FOV (blue regions) and the on-ground extended alias-free FOV (red regions) are given, respectively.

2) Angular Resolution: For an ASR, the angular resolution is a vital specification, which depends on the maximum dimension of the antenna array. The angular resolution at boresight can be approximately expressed by [21]

$$\Delta \xi_{-3dB}^{rect} \approx \frac{\pi/2}{\Delta u_{\max}} \qquad (5)$$

in which $\Delta u_{\max} = 2\sqrt{3} \cdot N_{el} \cdot d$ is the maximum baseline for "Y-shaped" array.

In addition, in accordance with the array factor of the "Y-shaped" array, the angular resolution of each pixel within the alias-free FOV can be estimated, and the on-ground spatial resolution of each pixel within the alias-free FOV can also be estimated. As shown in Fig. 8 (left), the on-ground spatial resolution of FPASMR is given. It can be seen that the spatial resolution is about 20∼65 km within alias-free FOV of L- and X-band ASR at the blackman window.

3) Radiometric Sensitivity: The snapshot radiometric sensitivity at boresight is expressed by [22], [23]

$$\Delta T_B = \Delta s \cdot \frac{T_A + T_R}{\sqrt{B \cdot \tau_{eff}}} \cdot \Omega_a \cdot \alpha_w \cdot \sqrt{N_v} \qquad (6)$$

in which Δs is the elementary area in u-v equal to $\sqrt{3}/2 \cdot d^2$, T_A and T_R are the antenna temperature and the receiver noise temperature, respectively. B is the noise equivalent bandwidth. τ_{eff} is the effective integration time, Ω_a is the antenna unit solid angle. α_w is the factor depending upon the apodization window. N_v is the number of u-v points considering their redundancy. The parameters in (6) are given in Table II. According to the parameters in Table II, the snapshot radiometric sensitivity at boresight is about 2.5 K for L-band ASR at the blackman window and 1.4 K for X-band ASR at the blackman window.
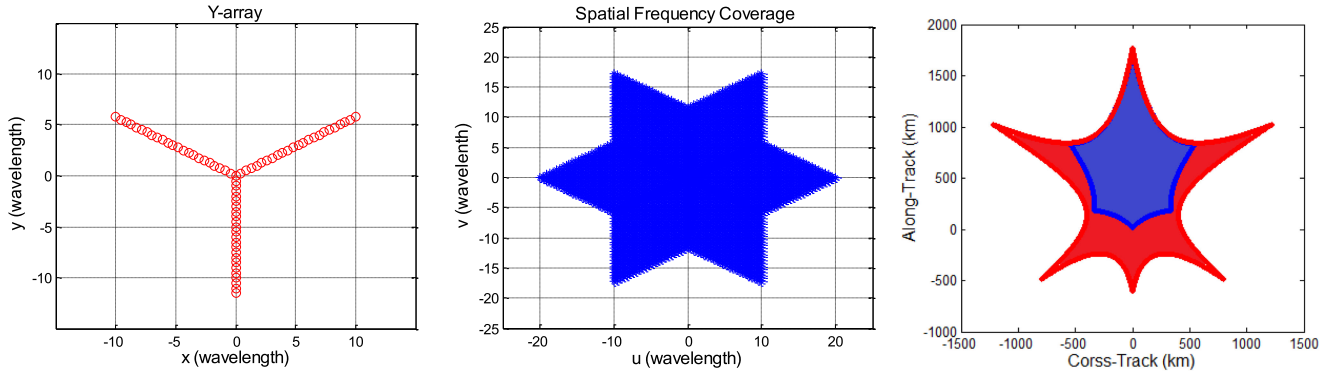
Fig. 7.   (Left) Antenna array of FPASMR. (Middle) The U-V coverage of FPASMR. (Right) The on-ground alias-free FOV (blue regions) and the on-ground extended alias-free FOV (red regions) of FPASMR.
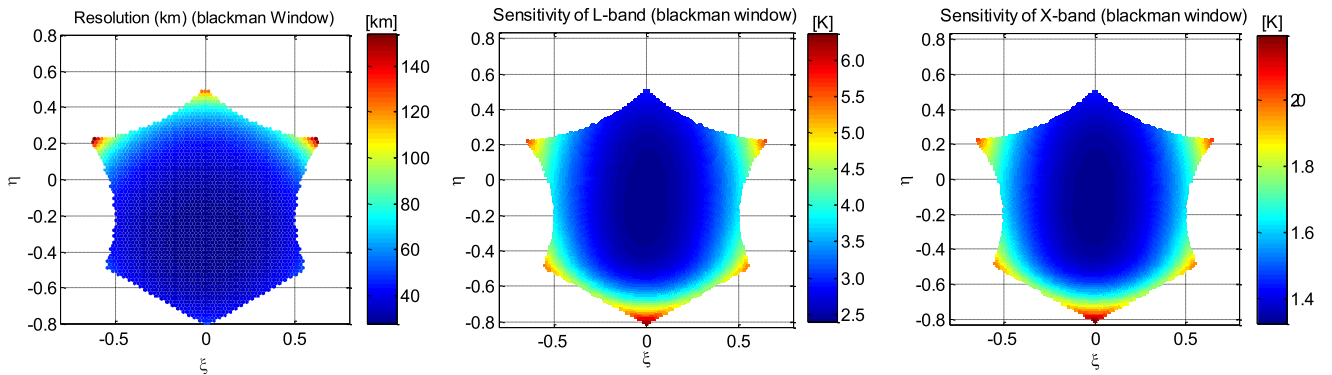

Fig. 8.   (Left) Resolution of FPASMR with blackman window. (Middle) Sensitivity of L-band ASR with blackman window. (Right) Sensitivity of X-band ASR with blackman window.

Considering the whole snapshot, the radiometric sensitivity is expressed by [23]

$$\Delta T_B = \Delta s \cdot \frac{F_n(\xi,\eta)}{\sqrt{1-\xi^2-\eta^2}} \cdot \frac{T_A+T_R}{\sqrt{B \cdot \tau_{eff}}} \cdot \Omega_a \cdot a_w \cdot \sqrt{N_v}$$

(7)

in which $(\xi,\eta) = (\sin\theta\cos\phi,\ \sin\theta\sin\phi)$ are the direction cosines, and $F_n(\xi,\eta)$ is the normalized antenna power pattern.

In accordance with (7) and the parameters listed in Table II, the radiometric sensitivity within the alias-free FOV can be estimated, and the results of the L- and X-band ASR in FPASMR are shown in Fig. 8 (middle) and Fig. 8 (right), respectively. It can be seen that the radiometric sensitivity within the alias-free FOV is about 2.5∼3.5 K for the L-band ASR at the blackman window and is about 1.4∼2.2 K for the X-band ASR at the blackman window.

C. FPASMR Calibration

Accurate calibration is very crucial to ensure the quality of the retrieved geophysical parameters for FPASMR. However, the end-to-end calibration is difficult to be performed for FPASMR due to the large antenna array in the L-band ASR. Thus, the calibration produce is divided into on-ground characterization and in-orbit calibration, as shown in Fig. 9.
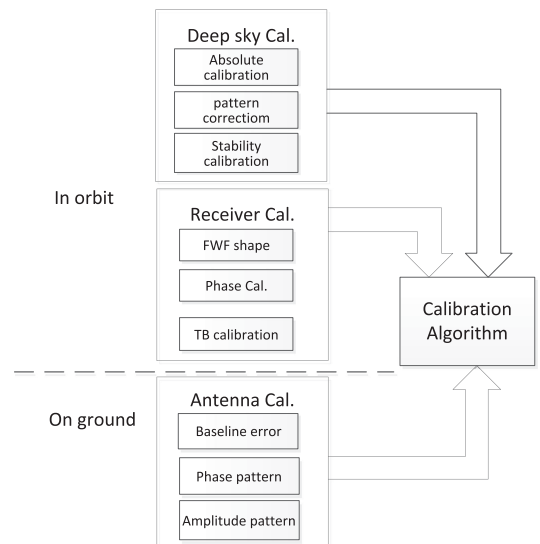

Fig. 9.   Calibration algorithm in FPASMR.

After FPASMR being launched, the in-orbit calibration is periodically performed, which contains the receiver calibration and the cold sky calibration. The in-orbit calibration is introduced in details as follow.
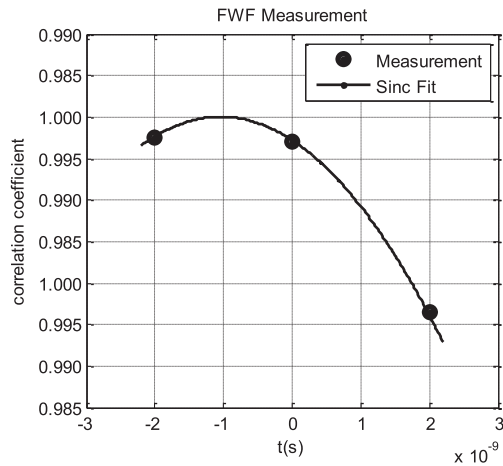
Fig. 10.   Measured FWF by three delay method.

1) Receiver Calibration: The receiver calibration contains the amplitude and phase calibration, the fringe-washing function (FWF), and the TB calibration.

1) Amplitude and phase calibration

Since the inconsistencies of the amplitude and phase of the receivers (called as the amplitude and phase errors) in the ASR have a serious negative impact on the measurement accuracy, the amplitude and phase calibrations are performed by injecting two levels of correlated noises in the receivers using the common noise source and the calibration network, and the phase and amplitude errors are estimated directly from the calibration measurements [24].

1) Fringe-washing function

A large ASR with a wide FOV usually suffers from severe decorrelation effects, so-called FWF, especially for the longest baseline [25]. The FWF has a negative impact on the TB measurement accuracy. Thus, the FWF must be accuracy measured for FPASMR, especially for the L-band ASR with large antenna array.

The FWF can be estimated by three delay method [25]. In the FPASMR, the correlated measurements are performed by simultaneously injecting correlated noises in the baselines with the delay $\tau = 0$ (punctual), $\tau = +T$ (early), and $\tau = -T$ (late). The FWFs at $\tau = 0$ (FWF(0)), $\tau = +T$ (FWF(+T)), and $\tau = -T$ (FWF(−T)) are estimated by the three correlated measurements, and the estimated FWF is fitted by FWF(0), FWF(+T), and FWF(−T). As shown in Fig. 10, FWF(0), FWF(+T), and FWF(−T) of one baseline in the L-band ASR are given as the black dots, and the fitted FWF based on the three measurements is also given as the black lines.

Since the digital filters and digital power measurement systems are employed in the L- and X-band ASR, the discrepancy of phase and amplitude of the receivers forming the baselines can be reduced to further mitigate the decorrelation effects, especially for the small baselines.

1) TB calibration

TB calibration is also referred as denormalization. The objective of TB calibration is to estimate the antenna temperature and system temperature of each receiver and de-normalize the visibilities for TB map reconstruction.

Fig. 11.   FPASMR demonstrator. (Left) The L-band subsystem demonstrator. (Right) The X-band subsystem demonstrator.

The antenna temperature and system temperature can be calibrated by the noise injection radiometer (NIR). NIR is a high accuracy and stability radiometers and will be calibrated by periodic (e.g., monthly) deep-sky views [16].

2) Deep Sky Calibration: After an ASR being launched in orbit, calibration parameters will drift with time and/or through orbital and seasonal variations, such as in SMOS [7]. The short-term drift calibration parameters (relative calibration) can be periodically recalibrated by the calibration subsystem, such as the amplitude and phase errors of the receivers. However, some calibration parameters suffer from long-term drifts and cannot be calibrated by the calibration subsystem, such as NIR, antenna pattern errors. For this reason, absolute calibration of the FPASMR instrument is periodically (e.g., monthly) performed by deep-sky views so as to calibrate NIR by the so-called one-point calibration [16]. During in the deep-sky views, the platform maneuvers to make the antenna arrays pointing toward to the cold space near the galactic poles [26]. In addition, during the deep-sky views, the flat target transformation is also performed to minimize the impacts from instrument errors, particularly antenna errors [27].

IV. VALIDATION, RESULTS, AND DISCUSSION

In this section, the FPASMR demonstrator is introduced and a series of experiments is performed to assess the performance of the FPASMR demonstrator and the improvements in the FPASMR.

A. FPASMR Demonstrator Description

The FPASMR demonstrator has also been designed as the similar system structure mentioned in Section III-A. In the FPASMR demonstrator, both L- and X-band subsystem employ a "Y-shaped" array with 6 antenna elements per each arm. The L- and X-band demonstrator are shown in Fig. 11. The main specifications of the L- and X-band demonstrators are given in Table III. In the following sections, a series of experiments is performed to assess main specifications of the FPASMR demonstrator.

The antenna patterns of the L- and X-band subsystem are accurately measured in a microwave anechoic chamber. As shown in Fig. 12, the single L-band antenna element and the measured normalized antenna power patterns are given. In addition, the antenna array in the L-band subsystem is measured in the spherical near field on ground, as shown in Fig. 13 (left), and the measured normalized antenna voltage pattern of one

TABLE III
SPECIFICATION OF DEMONSTRATOR

Subsystem	L-band	X-band
Antenna number	19	19
Center frequency	1.415 GHz	10.7 GHz
Bandwidth	20MHz	100MHz
Minimum spacing	~ 2.6 m	~0.3m
Integration time	1 s	1 s
Angular resolution at boresight	5.0$^\mathrm{o}$	5.0$^\mathrm{o}$
Extend FOV	≥50$^\mathrm{o}$	≥50$^\mathrm{o}$
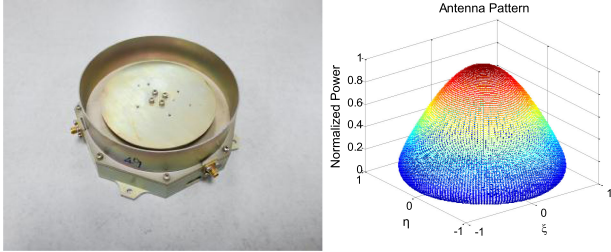
Fig. 12. (Left) L-band antenna element. (Right) The measurement normalized antenna power patterns.
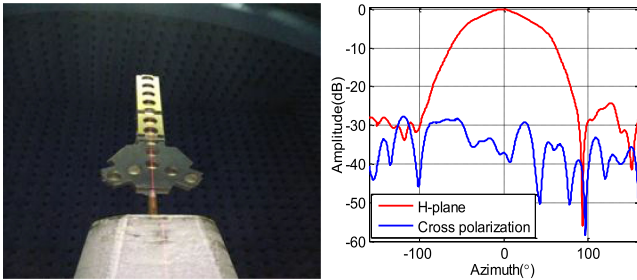
Fig. 13. (Left) Antenna array of the L-band subsystem in a microwave anechoic chamber. (Right) Measured antenna voltage pattern of one antenna.

antennae element is given in Fig. 13 (right). The antenna phase and amplitude patterns are accurately measured for the TB reconstruction. Baseline errors are also measured on ground.

B. Receiver Temperature Sensitivity

In SMOS, the results indicate that the physical temperature of the instruments show orbital variations and seasonal variations, which has a negative impact on the calibration accuracy and instrumental performance [27]. In this section, the temperature experiments are performance to assess the temperature sensitivity of the receivers and the temperature compensation method.

In the temperature experiments, an absolute calibration system manufactured by the Maury corporation (called as "Maury calibration system") provides a cold source (89 K) and a warm source (372 K) to calibrate the gain and offset of the receivers for absolute calibration, as shown in Fig. 14. The accuracy of the cold source and warm source is better than 0.1 K. The Maury calibration system can periodically inject noise sources that the cold source and the warm source into the receivers for absolute calibration.
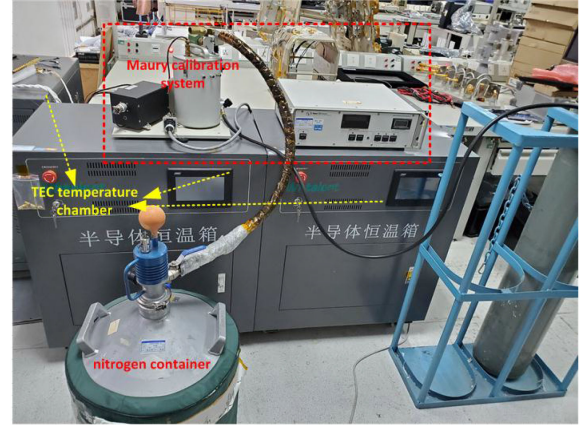

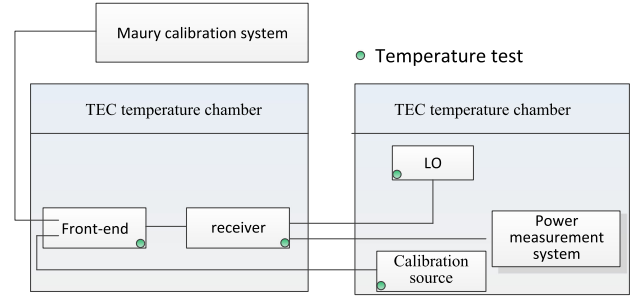Fig. 14. Maury calibration system and TEC temperature chambers in the experiments.

Fig. 15. Block diagram of the experiments of the receiver temperature sensitivity.

In addition, three thermo electric cooler (TEC) temperature chambers (see Fig. 14) can control the environment temperature of the receivers ranging from −5 °C∼55 °C, which is similar to the range of the orbital temperature variations. The controlled accuracy and measured accuracy of the TEC temperature chambers are better than 0.05 °C and 0.01 °C, respectively.

First, the sensitivity of the receivers over temperature is performed. In the experiment, only the receiver channel is in one TEC temperature chamber. The residual part is in another TEC temperature chamber with the constant temperature about 22 °C, such as LO. The block diagram of the experiments of the receiver temperature sensitivity is shown in Fig. 15. The TEC temperature chamber with the receiver slowly ranges from 16 °C to 36 °C. Meanwhile, the Maury calibration system periodically calibrates the gain and offset of the receivers in the experiments, and the physical temperatures of the receivers are estimated. The temperature sensitivity of the L- and X-band receiver are given Fig. 16 (top) and Fig. 16 (bottom), respectively, in which the black dots denote the measured data and the blue lines denotes the polynomial 2 fit lines. The on-ground measured sensitivities over temperature of the L- and X-band receiver will be used to compensate the in-orbit gain and offset drift over temperature.

C. Stability of Baselines in L- and X-Band ASR

The gain and phase stability of a baseline in L- and X-band are evaluated, respectively. In the experiments, the baseline formed
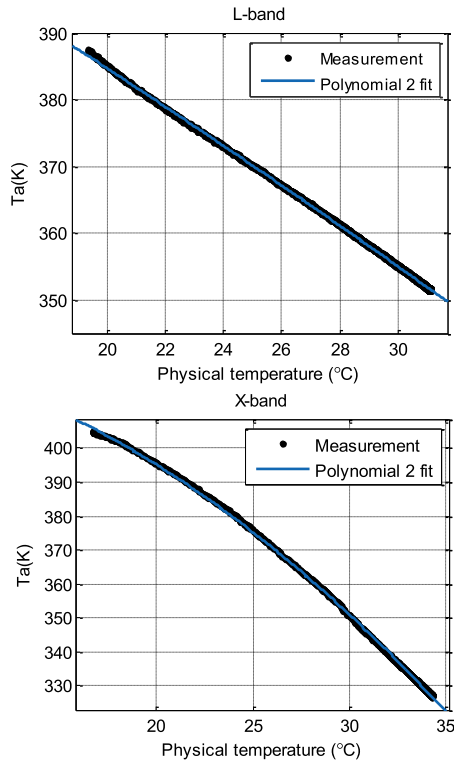
Fig. 16. Temperature sensitivity of the L-band receiver (top) and X-band receiver (bottom).

by two receivers in L- and X-band are installed on the TEC temperature chamber with a constant temperature about 34 °C in a peak to peak 0.15 °C. The physical temperature of the receivers is measured by the platinum resistance thermometers (PRT) with high accuracy. The calibration of the baselines in L- and X-band is also performed by the Maury calibration system. The durations of the experiments are about 5 days for L-band and 8 days for X-band, and the experimental results are given in Fig. 17. As shown in Fig. 17, the green dotted lines are the physical temperature of the receivers measured by a PRT. As shown in Fig. 17(a) and (c), the red dotted lines are the TB calibrated by the Maury calibration system, the black dotted lines is the temperature-compensated TB by the temperature compensation method in Section II-B, and the blue solid lines are the temperature-compensated move-averaged TB with 100 s. As shown in Fig. 17(b) and (d), the blue solid lines are the phase of the baselines in L- or X-band. It can be seen that the peak-to-peak of the temperature-compensated move-averaged TB with 100 s is about 0.09 K for L-band and about 0.016 K for X-band. The results indicate that the temperature compensation method is effective and the compensated move-averaged TB result exhibit a good stability. Meanwhile, the phase peak-to-peak variation of the baselines is about 0.08° in L-band and 0.12° in X-band, respectively. The results also indicate the phase of the baseline formed by two receivers exhibits a good stability.

Due to the large antenna array of the L- and X-band subsystem in FPASMR, an end-to-end simulator is established to assess the stability of FPASMR. In the end-to-end simulator, the main specifications of FPASMR and the aforementioned stability of

the receivers is considered as the input to assess the stability of FPASMR. As shown in Fig. 18, the relationship between the stability of the receivers and the stability of the L- and X-band subsystem in FPASMR is given. It can be seen that stability sensitivity of FPASMR over the stability of the receivers is 0.88 K/K for both L- and X-band subsystems. Based on stability sensitivity of FPASMR over the stability of the single receivers and the peak-to-peak of the temperature-compensated move-averaged TB, the stability of the FPASMR are about 0.079 K (0.09 × 0.88 K) for the L-band subsystem and about 0.014 K (0.016 × 0.88 K) for the X-band subsystem, respectively.

D. Experiments

A series of experiments is performed in an anechoic chamber to assess the sensitivity and calibration accuracy of the demonstrator. Due to the large antenna array of the L-band subsystem with 70 antennas, a demonstrator of the L-band subsystem with 19 antennas (6 antennas per each arm plus one antenna in hub) and the X-band subsystem with 19 antennas (6 antennas per each arm plus one antenna in hub) is considered to perform the experiments. In the anechoic chamber experiment, both L- and X-band subsystem point toward to a flat anechoic chamber wall. Due to the size limitation of the anechoic chamber, a small demonstrator of the L-band subsystem only with 7 antennas (2 antennas per each arm plus one antenna in hub) is performed to satisfy the far-filed condition in the anechoic chamber experiment. The integrate time of both subsystems is about 0.1 s, and many temperature sensors are installed to measure the physical temperature of the flat anechoic chamber wall. As shown in Fig. 19, the TB images of the flat anechoic chamber wall in L- and X-band are given at the blackman window, respectively. Meanwhile, the accuracy and sensitivity of the small demonstrator are evaluated by the TB images of the flat anechoic chamber wall for many times. The results indicate that the sensitivity is 0.20 K for L-band and 0.49 K for X-band at the blackman window, and the accuracy is 0.79 K for L-band and 1.35 K for X-band at the blackman window.

Meanwhile, the outdoor experiments are also performed. Since the L-band radiometers usually suffer serious radio frequency interference and the natural scenes cannot be clearly imaged by the L-band ASR, an artificial noise source is imaged by the L-band demonstrator. Due to the low angular resolution of the X-band demonstrator of about 7.2° at the blackman window, all TB maps of the scenes are retrieved by FFT with three-time zero-padded at the blackman window. As shown in Fig. 20, the TB images of an artificial noise source by L- and X-band demonstrator are given, respectively. A building is also observed by the X-band demonstrator. As shown in Fig. 21, the TB map and the optical image of the building are given. It can be seen that the shape of the building is clear in the observed TB map and shows a good agreement with the optical image.

Meanwhile, airborne experiments are also performed by the X-band demonstrator. In the airborne experiments, the X-band demonstrator is installed on the bottom of an aircraft, and the aircraft in the airborne experiment is shown in Fig. 22. In the experiments, the integrate time is 0.1 s, which can be adjusted
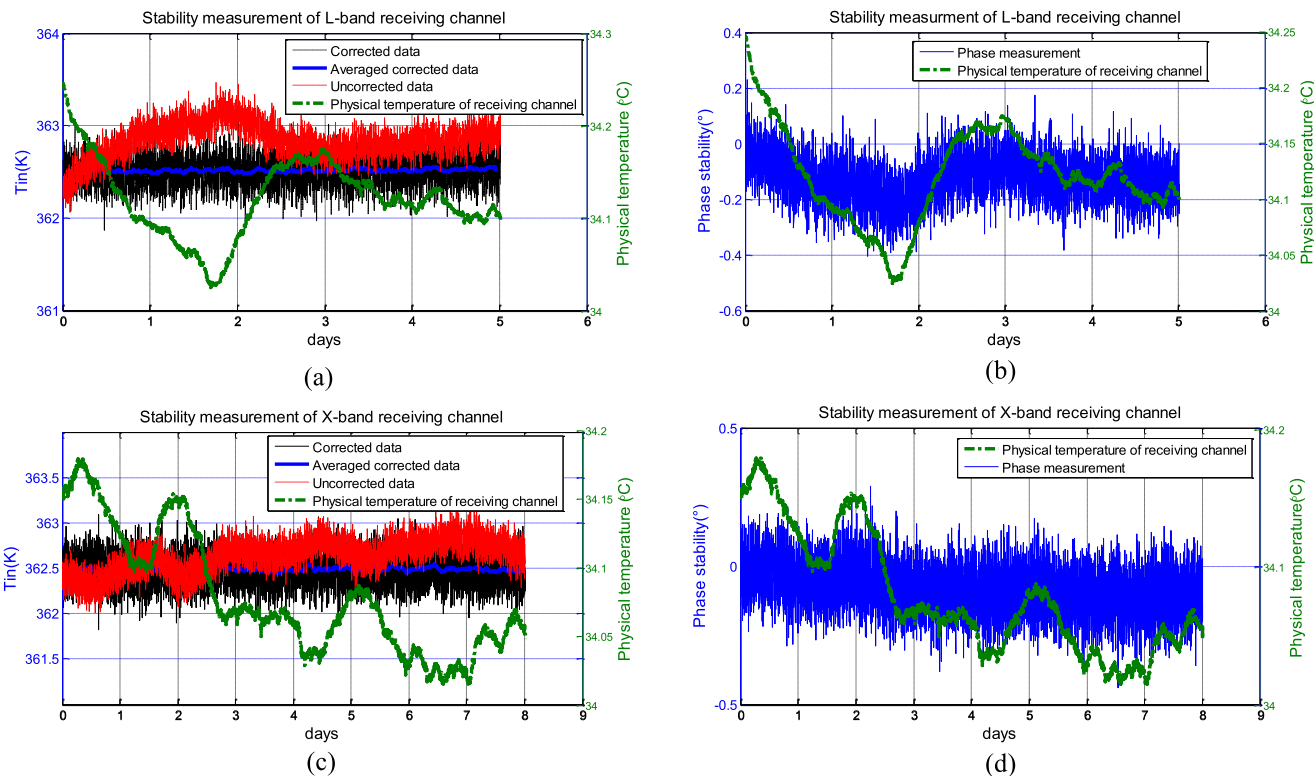
Fig. 17. Power and phase stability experiment of baselines in L- and X-band. (a) Power stability measurement of baselines in L-band. (b) Phase stability measurement of the baselines in L-band. (c) Power stability measurement of baselines in X-band. (d) Phase stability measurement of the baselines in X-band.
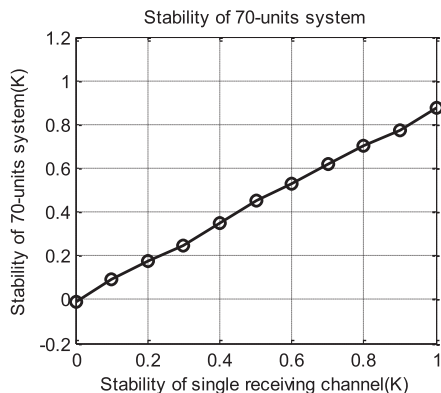

Fig. 18. Relationship between the stability of the single receivers and the stability of the L- and X-band subsystem.
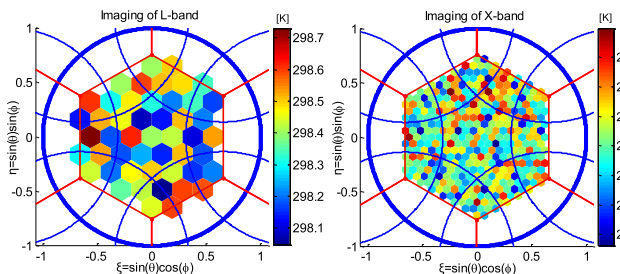

Fig. 19. Chamber wall TB images. (Left) The TB images of the flat anechoic chamber wall observed by L-band demonstrator. (Right) The TB images of the flat anechoic chamber wall observed by X-band demonstrator.
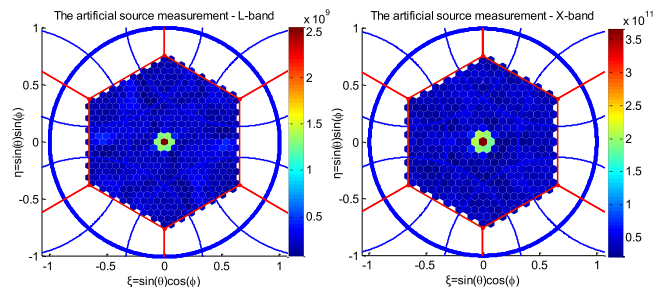

Fig. 20. TB images of an artificial source. (Left) The observed TB image of the artificial source by L-band demonstrator. (Right) The observed TB image of artificial source by X-band demonstrator.
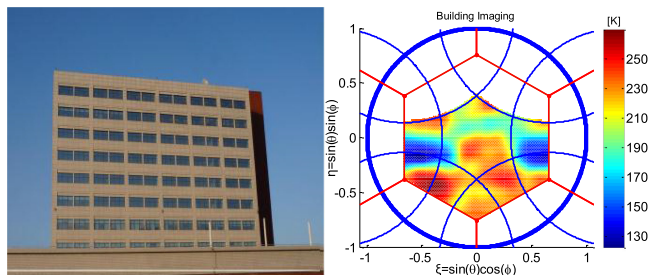

Fig. 21. (Left) Optical image of a building. (Right) The observed X-band TB image of a building.

as needed. The external calibration method and the internal calibration method are performed in the airborne experiments. The external calibration method aims to calibrate the amplitude
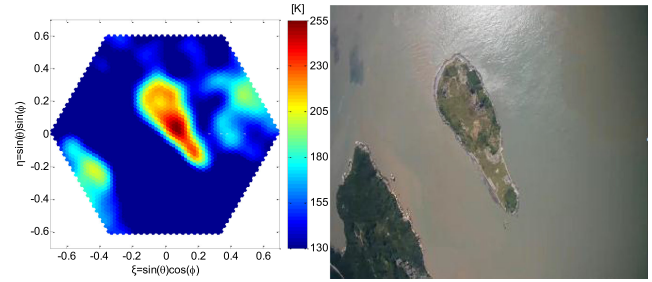
Fig. 22.   Aircraft in the airborne experiments.

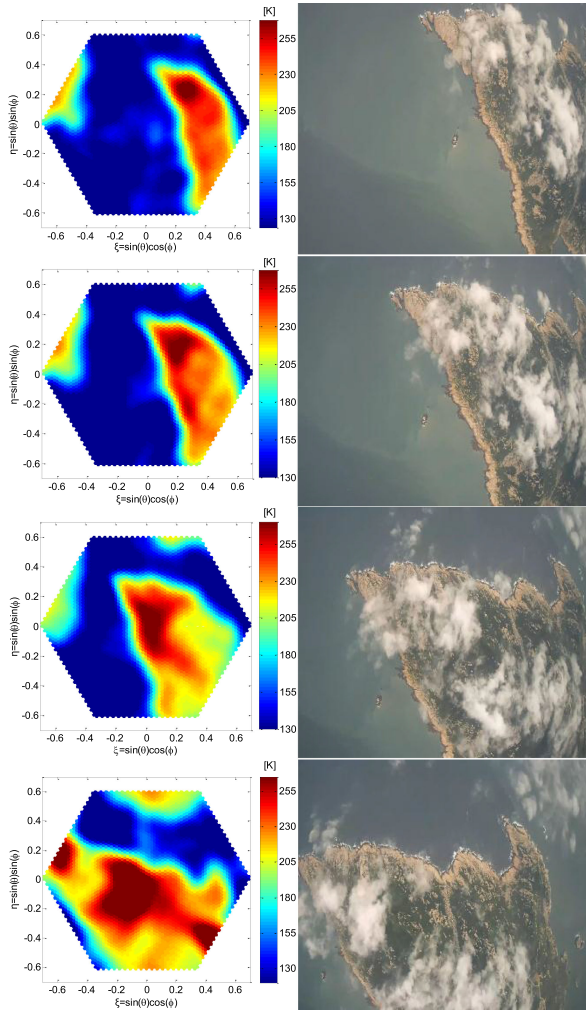Fig. 23.   (Left) Observed X-band TB images and (right) optical images of a large island.

Fig. 24.   (Left) Observed X-band TB image and (right) the optical image of a clavate island.
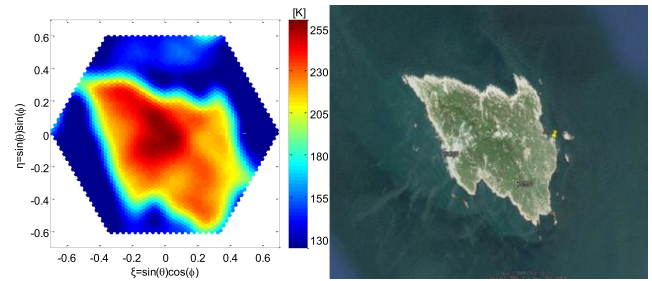

Fig. 25.   (Left) Observed X-band TB image in a cloudy weather and (right) the optical image of the large island in Fig. 23.

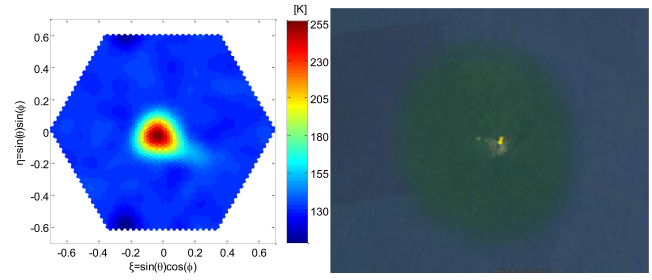Fig. 26.   (Left) Observed X-band TB image in a cloudy weather and (right) the optical image of a clavate small island.

and phase errors of the X-band subsystem, and the internal calibration method with two levels of correlated noises (warm and hot) and uncorrelated noises aims to calibrate the offset of the X-band subsystem and achieve absolute calibration. One airborne experiment is performed in a sunny weather. A large island is observed by the X-band demonstrator in the experiment. As shown in Fig. 23, the observed TB maps (left) and the optical images (right) of a large island are given, respectively. In addition, a clavate island is also observed by the X-band demonstrator, and the results are given in Fig. 24. It can be seen that the shapes of the islands are clear in the observed X-band maps,

which exhibit a good agreement with the optical images. It means that the X-band demonstrator exhibits a good performance in a sunny weather, as expected. Another airborne experiment is also performed in a cloudy weather. The large island in Fig. 23 is also observed by the X-band demonstrator in the cloudy weather. The observed TB map is shown in Fig. 25 (left), and the optical image from the Google Earth is also shown in Fig. 25 (right). The results demonstrate that the X-band demonstrator exhibits a good performance in the cloudy weather. In addition, a small island is also observed by the X-band demonstrator in the cloudy weather. The observed TB map and the optical image from the Google Earth are shown in Fig. 26 (left) and Fig. 26 (right), respectively. As shown in Fig. 26, the shape of the small island cannot be clearly seen due to the poor angular resolution.

In addition, the sensitivity of the X-band demonstrator is assessed. The sea surface TB varies smoothly within tens of kilometers in the open ocean, the observed TB maps of the sea surface from the air are also considered to be almost the same within ten kilometers in the open ocean. Thus, the standard
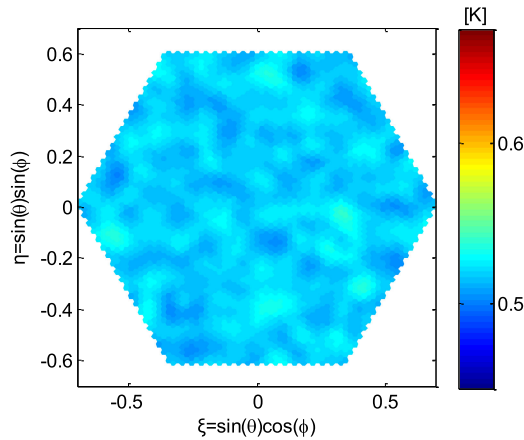
Fig. 27. Standard deviation of the observed TB maps in an open ocean.

deviation of the observed TB maps within ten kilometers in the open ocean is considered to assess the sensitivity of the X-band subsystem, which includes the additional noises caused by the fluctuations of the aircraft [28]. As shown in Fig. 27, the standard deviation of the observed TB maps in an open ocean is given. It can be seen that standard deviation of the observed X-band TB maps is about 0.52 K in the open ocean, which is within the theoretical result about 0.44~0.70 K and is slightly higher than the sensitivity of the X-band subsystem about 0.49 K in the anechoic chamber experiment.

V. CONCLUSION

To further improve SSS accuracy, FPASMR has been developed by the China Academy of Space Technology (Xi'an) with two important improvements for China's next-generation HY satellite program. One important improvement is that SSR and SST are simultaneously measured by the full polarization X-band ASR to reduce the wind speed errors and SST measurement errors. Another important improvement is that the microwave-optical receiving technology and in-orbit thermal control subsystem are employed in FPASMR to reduce the visibility phase errors by improving the stability of the instruments. In addition, a temperature compensation method is considered. FPASMR is composed by an L-band 2-D ASR and an X-band 2-D ASR. Both ASRs employ the "Y-shaped" array with 23 antennas per arm plus one in the center. A centralized calibration subsystem is considered with two levels of correlated noises and un-correlated noises. The spatial resolutions of the L- and X-band ASR are about 20~65 km at the altitude of 655 km and the tilt angle of 30°. The radiometric sensitivity within the alias-free FOV is about 2.5~3.5 K for the L-band ASR and is about 1.4~2.2 K for the X-band ASR. FPASMR calibration is introduced, which comprises the on-ground characterization and in-orbit calibration.

In addition, the FPASMR demonstrator has been developed and a series of experiments is performed to assess its performance and improvements. The temperature sensitivities of the L- and X-band receiver are estimated and the temperature compensation method is performed. The results indicate that the temperature compensation method is effective and the phases of the baselines (visibilities) in L- and X-band exhibit a good stability. The stability of the baselines (visibilities) in FPASMR is estimated to be 0.079 K for the L-band subsystem and 0.014 K for the X-band subsystem, respectively. Meanwhile, experiments in an anechoic chamber are performed to assess its sensitivity and calibration accuracy. The results indicate that the sensitivity is 0.20 K for L-band and 0.49 K for X-band in the FPASMR demonstrator, and the accuracy is 0.79 K for L-band and 1.35 K for X-band in FPASMR demonstrator. Outdoor experiments are also performed to assess the performance of the L- and X-band ASR in the FPASMR demonstrator, which comprise the imaging experiments of the artificial noise source and the building, and the airborne experiments. The building and the large islands can be seen clearly in the observed TB map by the X-band demonstrator. The results indicate that the standard deviation of the observed X-band TB maps is about 0.52 K in the open ocean, which is within the theoretical result about 0.44~0.70 K and is slightly higher than the sensitivity of the X-band subsystem about 0.49 K in the anechoic chamber experiment.

As mentioned in [28], since the fluctuations of the aircraft cause additional noises in the observed TB maps, the sensitivity of the X-band subsystem cannot be accurately estimated. Meanwhile, since the TB of the flat open ocean is unknown, the calibration accuracy of the X-band subsystem can also not be accurately estimated. In addition, due to the large volume of the L-band subsystem and the volume limitation of the aircraft, the L-band subsystem is not performed together with the X-band subsystem in the airborne experiments to evaluate the improvements of X-band subsystem for SSS retrieved accuracy by L-band subsystem, which will be considered in further work.

ACKNOWLEDGMENT

REFERENCES

[1] G. S. E. Lagerloef, "Introduction to the special section: The role of surface salinity on upper ocean dynamics, air-sea interaction and climate," *J. Geophysical Res.*, vol. 107, no. C12, pp. SRF1–SRF1–2.

[2] H. Barré, B. Duesmann, and Y. Kerr, "SMOS: The mission and the system," *IEEE Trans. Geosci. Remote Sens.*, vol. 46, no. 3, pp. 587–593, Mar. 2008.

[3] D. M. Le Vine, G. S. E. Lagerloef, F. R. Colomb, S. H. Yueh, and F. A. Pellerano, "Aquarius: An instrument to monitor sea surface salinity from space," *IEEE Trans. Geosci. Remote Sens.*, vol. 45, no. 7, pp. 2040–2050, Jul. 2007.

[4] J. Boutin *et al.*, "New SMOS sea surface salinity with reduced systematic errors and improved variability," *Remote Sens. Environ.*, vol. 214, pp. 115–134, Sep. 2018.

[5] D. Gomis and G. Jorda, "Accuracy of SMOS level 3 SSS products related to observational errors," *IEEE Trans. Geosci. Remote Sens.*, vol. 48, no. 4, pp. 1694–1701, Apr. 2010.

[6] H. Lu *et al.*, "An L-band phased array radiometer for sea surface salinity in coastal zones," *IEEE J. Sel. Topics Appl. Earth Observ. Remote Sens.*, vol. 14, pp. 1520–1531, Jan. 2021.

[7] M. Martín-Neira *et al.*, "SMOS instrument performance and calibration after six years in orbit," *Remote Sens. Environ.*, vol. 180, pp. 19–39, Jul. 2016.

[8] I. Corbella *et al.*, "Impact of the local oscillator calibration rate on the SMOS measurements and retrieved salinities," *IEEE Trans. Geosci. Remote Sens.*, vol. 51, no. 9, pp. 4633–4642, May 2013.

[9] X. Yina, J. Boutina, N. Martina, J. L. Vergely, and F. Gaillard, "Errors in SMOS sea surface salinity and their dependency on a priori wind speed," *Remote Sens. Environ.*, vol. 146, pp. 159–171, Apr. 2014.

[10] X. Yina, J. Boutin, E. Dinnat, Q. Song, and A. Martin, "Roughness and foam signature on SMOS-MIRAS brightness temperatures: A semi-theoretical approach," *Remote Sens. Environ.*, vol. 180, pp. 221–233, Jul. 2016.

[11] Y. Li *et al.*, "FPASMR: A L\X-band full polarization aperture synthesis microwave radiometer," in *Proc. IEEE Int. Geosci. Remote Sens. Symp.*, Jul. 2013, pp. 1920–1923.

[12] T. Meissner, F. Wentz, and L. Ricciardulli, "The emission and scattering of L-band microwave radiation from rough ocean surfaces and wind speed measurements from the Aquarius sensor," *J. Geophys. Res.*, vol. 119, no. 9, pp. 6499–6522, Sep. 2014.

[13] Y. Kerr *et al.*, "The SMOS mission: New tool for monitoring key elements of the global water cycle," *Proc. IEEE*, vol. 98, no. 5, pp. 666–687, May 2010.

[14] S. H. Yueh, R. West, W. J. Wilson, F. K. Li, E. G. Njoku, and Y. Rahmat-Samii, "Error sources and feasibility for microwave remote sensing of ocean surface salinity," *IEEE Trans. Geosci. Remote Sens.*, vol. 39, no. 5, pp. 1049–1059, May 2001.

[15] P. A. Hwang, "Surface foam and L-band microwave radiometer measurements in high winds," *IEEE Trans. Geosci. Remote Sens.*, vol. 57, no. 5, pp. 2766–2776, May 2019.

[16] M. A. Brown, F. Torres, I. Corbella, and A. Colliander, "SMOS calibration," *IEEE Trans. Geosci. Remote Sens.*, vol. 46, no. 3, pp. 646–658, Mar. 2008.

[17] I. Corbella *et al.*, "On-ground characterization of the SMOS payload," *IEEE Trans. Geosci. Remote Sens.*, vol. 47, no. 9, pp. 3123–3133, Sep. 2009.

[18] F. Torres *et al.*, "Denormalization of visibilities for in-orbit calibration of interferometric radiometers," *IEEE Trans. Geosci. Remote Sens.*, vol. 44, no. 10, pp. 2679–2686, Oct. 2006.

[19] K. D. McMullan *et al.*, "SMOS: The payload," *IEEE Trans. Geosci. Remote Sens.*, vol. 46, no. 3, pp. 594–605, Mar. 2008.

[20] A. Camps, X. Bosch-Lluis, I. Ramos-Perez, J. F. Marchan, B. Izquierdo, and N. Rodriguez, "New instrument concepts for ocean sensing: Analysis of the PAU radiometer," *IEEE Trans. Geosci. Remote Sens.*, vol. 45, no. 10, pp. 3180–3192, Oct. 2007.

[21] A. Camps, J. Bara, I. Corbella, and F. Torres, "The processing of hexagonally sampled signals with standard rectangular techniques: Application to 2-D large aperture synthesis interferometric radiometers," *IEEE Trans. Geosci. Remote Sens.*, vol. 35, no. 1, pp. 183–190, Jan. 1997.

[22] A. Camps, "Application of interferometric radiometry to earth observation," Ph.D. dissertation, Univ. Politecnica de Catalunya, Barcelona, Spain, Nov. 1996.

[23] A. Camps, I. Corbella, J. Bará, and F. Torres, "Radiometric sensitivity computation in aperture synthesis interferometric radiometry," *IEEE Trans. Geosci. Remote Sens.*, vol. 36, no. 2, pp. 680–685, Mar. 1998.

[24] I. Corbella *et al.*, "MIRAS end-to-end calibration: Application to SMOS L1 processor," *IEEE Trans. Geosci. Remote Sens.*, vol. 43, no. 5, pp. 1126–1134, May 2005.

[25] R. Butora, M. Martin-Neira, and A. Rivada, "Fringe-washing function calibration in aperture synthesis microwave radiometry," *Radio Sci.*, vol. 38, no. 2, pp. 15-1–15-15, Apr. 2003.

[26] D. M. Le Vine and S. Abraham, "Galactic noise and passive microwave remote sensing from space at L-band," *IEEE Trans. Geosci. Remote Sens.*, vol. 42, no. 1, pp. 119–129, Jan. 2004.

[27] M. Martín-Neira, M. Suess, and J. Kainulainen, "The flat target transformation," *IEEE Trans. Geosci. Remote Sens.*, vol. 46, no. 3, pp. 613–620, Mar. 2008.

[28] H. Lu *et al.*, "A ship detection and tracking algorithm for an airborne passive interferometric microwave sensor (PIMS)," *IEEE J. Sel. Topics Appl. Earth Observ. Remote Sens.*, vol. 14, pp. 3519–3532, Mar. 2021.